Higher Order Hybrid Method of Moments–Physical Optics Modeling Technique for Radiation and Scattering From Large Perfectly Conducting Surfaces

Miroslav Djordjević, *Member, IEEE,* and Branislav M. Notaroš, *Senior Member, IEEE*

***Abstract*—An efficient and accurate higher order, large-domain hybrid computational technique based on the method of moments (MoM) and physical optics (PO) is proposed for analysis of large antennas and scatterers composed of perfectly conducting surfaces of arbitrary shapes. The technique utilizes large generalized curvilinear quadrilaterals of arbitrary geometrical orders in both the MoM and PO regions. It employs higher order divergence-conforming hierarchical polynomial basis functions in the context of the Galerkin method in the MoM region and higher order divergence-conforming interpolatory Chebyshev-type polynomial basis functions in conjunction with a point-matching method in the PO region. The results obtained by the higher order MoM-PO are validated against the results of the full MoM analysis in three characteristic realistic examples. The truly higher order and large-domain nature of the technique in both MoM and PO regions enables a very substantial reduction in the number of unknowns and increase in accuracy and efficiency when compared to the low-order, small-domain MoM-PO solutions. The PO part of the proposed technique, on the other hand, allows for a dramatic reduction in the computation time and memory with respect to the pure MoM higher order technique, which greatly extends the practicality of the higher order MoM with a smooth transition between low- and high-frequency applications.**

***Index Terms*—Electromagnetic analysis, higher order modeling, hybrid methods, method of moments (MoM), physical optics (PO), reflector antennas.**

I. Introduction

THE method of moments (MoM) for discretizing integral equations in electromagnetics is an extremely powerful and versatile general numerical methodology for electromagnetic-field simulation in antenna and scattering applications [1]. However, traditional MoM analysis is inherently limited to electrically small and moderately large electromagnetic structures, because its computation costs (in terms of memory and CPU time) increase rapidly with an increase in electrical size of the problem. Modern radio, wireless, and satellite communication and radar systems, on the other hand, often involve electrically very large metallic surfaces, that span many wavelengths in three dimensions and may possess arbitrary curvature. Most frequently, major parts of these surfaces are smoothly curved (on the scale of the wavelength), so that they can be approximated as locally planar. Therefore, one strategy to substantially reduce the computation time and memory requirements at high frequencies is based on a hybridization of the MoM, which is a numerically exact method, with numerically approximate high-frequency techniques [2], [3] for asymptotic analysis of electrically very large smooth parts of the structure. With this, the applicability of MoM may be extended to analysis of a wide class of large-scale practical electromagnetic problems. The overall accuracy of the analysis can be kept high by rigorously treating (by MoM) all nonsmooth parts of the structure that exhibit singular or resonant behavior and are expected to introduce significant errors if in the asymptotic region (e.g., electrically small and resonant surfaces, parts near edges and wedges, etc.).

MoM can be hybridized with either ray-based high-frequency asymptotic techniques, such as the uniform geometric theory of diffraction (UTD) [3], or current-based high-frequency asymptotic methods, such as the physical optics (PO) [3]. When some regions of an arbitrary complex structure have to be treated with the MoM and the remaining parts by an asymptotic technique, combining MoM with a current-based asymptotic technique is a preferable choice since MoM is based on currents as well. For instance, with such purely current-based hybrid method, a continuous current flow can be modeled on the entire surface of the object.

Several current-based hybrid general methods have been proposed and used for modeling of three-dimensional (3-D) metallic radiation and scattering structures over the last several years [4]–[11]. The fundamental shortcoming of the existing methods is the adopted low-order current approximation, which implies that the surface elements for modeling the structure geometry must be electrically very small, that is, on the order of $\lambda/10$ in each dimension, where λ is the free-space wavelength. This gives rise to small-domain (low-order) MoM-PO computational techniques and results in a very large number of unknowns (unknown current-distribution coefficients) required to obtain results of satisfactory accuracy, with all the associated problems, and still considerably limits the applicability and effectiveness of the hybrid approach in real-world radiation/scattering problems. In specific, the existing hybrid MoM-PO methods use

Manuscript received July 2, 2003; revised June 13, 2004. This work was supported by the National Science Foundation under Grant ECS-0115756.

M. Djordjević was with the Department of Electrical and Computer Engineering, University of Massachusetts Dartmouth, Dartmouth, MA 02747-2300. He is now with Antenna Research Associates, Incorporated, Beltsville, MD 20705 USA (e-mail: miroslav@ieee.org).

B. M. Notaroš is with the Department of Electrical and Computer Engineering, University of Massachusetts Dartmouth, Dartmouth, MA 02747-2300 USA (e-mail: bnotaros@umassd.edu).

Digital Object Identifier 10.1109/TAP.2004.841318

Rao–Wilton–Glisson (RWG) rooftop basis functions [12] defined on triangular patches, which are normally on the order of $\lambda^2/100$ in area, for the approximation of currents over metallic surfaces in both the MoM- and PO-regions and 1-D rooftop functions (piecewise linear expansion) for the approximation of the current intensity along wires. A notable example of using large surface elements in the PO region is the hybrid technique proposed in [13], where the low-order RWG scheme over PO elements has been improved and a significant reduction in the required number of PO unknowns achieved by implementing a linear phase interpolation over large triangular patches. Only very recently, higher order MoM-PO methods have been proposed [14], [15] that show great potential for dramatically reducing the number of unknowns for a given problem and enhancing further the accuracy and efficiency of the MoM-PO analysis in practical applications.

This paper proposes an efficient and accurate higher order, large-domain PC-oriented hybrid MoM-PO technique for 3-D analysis of arbitrary perfectly conducting antennas and scatterers in frequency domain. In general, the higher order, large-domain approach in computational electromagnetics utilizes higher order expansion functions defined in electrically relatively large elements (e.g., [16]–[19]). Theoretical foundation of the hybrid technique is a system of coupled surface integral equations, with an electric field integral equation (EFIE) in the exact (MoM) part of the structure under consideration and a magnetic field integral equation (MFIE) in the asymptotic (PO) part of the structure [5]. The PO approximation for surface currents is employed in the asymptotic region, which is assumed to be composed of smooth large surfaces. The proposed technique represents a generalization and extension of the higher order Galerkin-type MoM [19], which is referred to as a double-higher order method because it combines higher order geometrical modeling and higher order current modeling. Within the presented MoM-PO method, all the surfaces in the system, in both the MoM and PO regions, are modeled by electrically large generalized curvilinear quadrilaterals of arbitrary geometrical orders (large domains). Different higher order divergence-conforming basis and testing functions are used in the MoM and PO regions of the structure, in order to maximize the overall efficiency and accuracy of the hybrid method. In the MoM region, basis functions are higher order hierarchical polynomials of the parametric coordinates over generalized quadrilaterals that automatically satisfy continuity boundary conditions for the current components normal to the quadrilateral edges shared by adjacent elements in the model (divergence conformity) and the same functions are used for testing (Galerkin technique). In the PO region, basis functions are higher order divergence-conforming interpolatory polynomials based on modified Chebyshev polynomials of parametric coordinates and the testing procedure is a modified point-matching technique at the interpolation points of the basis functions. Some preliminary results of our higher order MoM-PO modeling are given in [15].

Because the adopted quadrilateral patches have both higher order geometrical flexibility for curvature modeling and higher order current-approximation flexibility for current modeling, large curved quadrilaterals that are on the order of λ (e.g., $1\lambda - 2\lambda$) in each dimension can be used as building blocks for modeling of the electromagnetic structure. This means that the surface elements can be by two orders of magnitude larger in area than traditional low-order patches, which greatly reduces the overall number of unknowns and significantly enhances the performance of the technique, as compared to traditionally used low-order basis functions in MoM-PO modeling. In addition, the choice of higher order hierarchical polynomials in the MoM region allows for a whole spectrum of element sizes and "regular" and "irregular" element shapes, with the corresponding current-approximation orders, to be used at the same time in a single simulation model of a complex structure. This enables a very efficient nonuniform selective discretization of the MoM solution domain. On the other side, the proposed interpolatory polynomials and conformal point-matching testing in the PO region make possible that the extremely large PO-PO projection matrix in the general EFIE/MFIE matrix equation for a structure be made an identity matrix, which tremendously reduces the computational costs associated with electromagnetic interactions in the PO region. This is crucial for the overall efficiency of the hybrid method. Finally, this particular choice of basis and testing functions in the PO region enables junctions of generalized quadrilaterals with different current-approximation orders, which yields the same flexibility in discretizing the surfaces as in the MoM region.

Due to its PO extension, the proposed hybrid higher order MoM-PO method is much more efficient in analysis of large metallic structures than its pure MoM counterpart [19]. Due to its truly higher order and large-domain nature in both MoM and PO regions, on the other hand, the presented hybrid method is much more efficient than the existing hybrid MoM-PO techniques [4]–[11], which are based on low-order, small-domain discretization of both MoM and PO regions.

This paper is organized as follows. Section II presents the theoretical background and numerical components of the higher order hybrid MoM-PO method. This includes the derivation of the hybrid MoM-PO system of electric and magnetic surface integral equations for unknown surface electric currents in the structure with the PO approximation in the asymptotic region and representation of this system in matrix form, geometrical modeling of MoM and PO surfaces by curved generalized quadrilaterals, development of higher order basis and testing functions for the MoM and PO region, respectively, and evaluation of MoM-PO interaction impedance and projection matrices for higher order quadrilateral elements and the proposed basis and testing functions. In Section III, numerical examples showing excellent efficiency and accuracy of the proposed technique at modeling of radiation systems that include flat and curved large surfaces are an array of dipoles in front of a large metallic cylinder, a monopole antenna attached to a large metallic plate, and a parabolic reflector antenna with a pyramidal horn feed.

II. Higher Order Hybrid MoM—PO Technique

A. Hybrid MoM-PO System of Electric and Magnetic Surface Integral Equations

Consider an electromagnetic structure consisting of arbitrarily shaped metallic surfaces and wires. Let the structure be excited by a time-harmonic electromagnetic field of complex field-intensities $\boldsymbol{E}^{\mathrm{i}}$ and $\boldsymbol{H}^{\mathrm{i}}$, and angular frequency ω. This

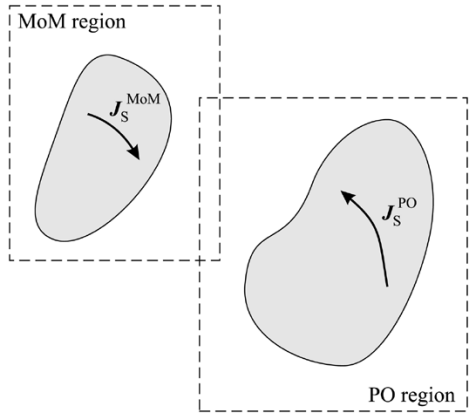

Fig. 1. Decomposition of an electromagnetic structure into a MoM and a PO region.

field may be a combination of incident plane waves (for a scattering structure) or the impressed field of one or more lumped generators (for an antenna structure). Our primary goal is to numerically evaluate the distribution of surface electric currents in the structure. The analysis can be performed using the MoM alone. However, at higher frequencies, significant reductions in memory requirements and computation time can be achieved if high-frequency approximations, such as the PO method, are employed on electrically large, smooth parts of the structure. To this end, we hybridize the MoM and the PO method, both as truly higher order computational techniques.

As the first step, we decompose the structure under consideration into two parts: a MoM region and a PO region (Fig. 1). The surface current density vectors in the MoM and PO regions are denoted by $\boldsymbol{J}_{\mathrm{S}}^{\mathrm{MoM}}$ and $\boldsymbol{J}_{\mathrm{S}}^{\mathrm{PO}}$, respectively. Note that, as the two regions are separated only in the basis-functions space, they can be physically connected or even overlap.

The currents in both the MoM and PO regions are the sources of scattered electric and magnetic fields, of intensities $\boldsymbol{E}$ and $\boldsymbol{H}$. The boundary conditions for the tangential components of the total (incident plus scattered) electric and magnetic field vectors on the metallic (perfectly conducting) surfaces in the model can be written as

$$\boldsymbol{n}\times\left[\boldsymbol{E}\left(\boldsymbol{J}_{\mathrm{S}}^{\mathrm{MoM}}\right)+\boldsymbol{E}\left(\boldsymbol{J}_{\mathrm{S}}^{\mathrm{PO}}\right)+\boldsymbol{E}^{\mathrm{i}}\right]=0 \quad \text{(EFIE)} \tag{1}$$

$$\boldsymbol{J}_{\mathrm{S}}^{\mathrm{PO}}+\boldsymbol{J}_{\mathrm{S}}^{\mathrm{MoM}}=2\boldsymbol{n}\times\left[\bar{\boldsymbol{H}}\left(\boldsymbol{J}_{\mathrm{S}}^{\mathrm{MoM}}\right)+\bar{\boldsymbol{H}}\left(\boldsymbol{J}_{\mathrm{S}}^{\mathrm{PO}}\right)+\boldsymbol{H}^{\mathrm{i}}\right] \quad \text{(MFIE)} \tag{2}$$

where $\boldsymbol{n}$ is the unit normal vector on the surface, and $\bar{\boldsymbol{H}}$ is the average value of $\boldsymbol{H}$ as the surface is approached from the opposite sides, i.e., at points just above and below the surface. For $\boldsymbol{E}$, such averaging is not necessary, since the tangential scattered electric field is continuous at the surface. The first condition, which represents an electric field integral equation (EFIE), is applied on surfaces in the MoM region. The second condition represents the magnetic field integral equation (MFIE) and is imposed over surfaces in the PO region. Note that the term $\boldsymbol{J}_{\mathrm{S}}^{\mathrm{MoM}}$ on the left-hand side of (2) is nonzero only if there is an overlapping between the MoM and PO current-domains, for current expansion functions defined on surface elements that are geometrically on the PO surfaces but computationally belong to the MoM current-domain in order to enforce the current-continuity condition across the boundary between the MoM and PO regions.

The scattered electric and magnetic fields are expressed via the magnetic vector potential, $\boldsymbol{A}$, and the electric scalar potential, Φ, in a standard fashion:

$$\boldsymbol{E}(\boldsymbol{J}_{\mathrm{S}})=-\mathrm{j}\omega\boldsymbol{A}-\nabla\Phi \tag{3}$$

$$\bar{\boldsymbol{H}}(\boldsymbol{J}_{\mathrm{S}})=\frac{1}{\mu}\bar{\nabla}\times\boldsymbol{A}. \tag{4}$$

The operator $\bar{\nabla}$ signifies that, for the field points lying in the current sheet $\boldsymbol{J}_{\mathrm{S}}$ (thus coinciding with the source points), $\bar{\nabla}\times\boldsymbol{A}$ is determined as the average value of $\nabla\times\boldsymbol{A}$ on both sides of the current sheet, close to the surface (for other field points, $\bar{\nabla}\equiv\nabla$). For $\nabla\Phi$, the averaging is not necessary, as we are interested only in the tangential component of $\boldsymbol{E}$ in (1). The potentials, in turn, are obtained by the following expressions in terms of the current density:

$$\boldsymbol{A}=\mu\int_S \boldsymbol{J}_{\mathrm{S}}g\,\mathrm{d}S, \tag{5}$$

$$\Phi=\frac{\mathrm{j}}{\omega\varepsilon}\int_S \nabla_{\mathrm{S}}\cdot\boldsymbol{J}_S g\,\mathrm{d}S \tag{6}$$

where S represents all the surfaces in the system. Green's function is given by

$$g=\frac{\mathrm{e}^{-\gamma R}}{4\pi R},\quad \gamma=\mathrm{j}\omega\sqrt{\varepsilon\mu} \tag{7}$$

with R being the distance of the field point from the source point and ε and μ the permittivity and permeability of free space.

In the hybrid MoM-PO method, MFIE (2) is solved using the PO approximation for the surface currents, which inherently neglects mutual interaction effects within the currents in the PO region and imposes the geometrical-optics shadow condition, thus reducing (2) to (8), shown at the bottom of the page. Combined with the integral expressions for the electric and magnetic fields (3)–(7), the EFIE/MFIE system of equations can now be rewritten as

$$\boldsymbol{n}\times\left[-\mathrm{j}\omega\mu\int_S\left(\boldsymbol{J}_{\mathrm{S}}^{\mathrm{MoM}}+\boldsymbol{J}_{\mathrm{S}}^{\mathrm{PO}}\right)g\,\mathrm{d}S-\frac{\mathrm{j}}{\omega\varepsilon}\nabla\int_S\nabla_{\mathrm{S}}\cdot\left(\boldsymbol{J}_{\mathrm{S}}^{\mathrm{MoM}}+\boldsymbol{J}_{\mathrm{S}}^{\mathrm{PO}}\right)g\,\mathrm{d}S+\boldsymbol{E}^{\mathrm{i}}\right]=0 \tag{9}$$

$$\boldsymbol{J}_{\mathrm{S}}^{\mathrm{MoM}}+\boldsymbol{J}_{\mathrm{S}}^{\mathrm{PO}}=\begin{cases}2\boldsymbol{n}\times\left[\bar{\boldsymbol{H}}\left(\boldsymbol{J}_{\mathrm{S}}^{\mathrm{MoM}}\right)+\boldsymbol{H}^{\mathrm{i}}\right], & \text{in the lit PO region}\\ 0, & \text{in the shadowed PO region}\end{cases} \tag{8}$$

$$\boldsymbol{J}_{\mathrm{S}}^{\mathrm{PO}}+\boldsymbol{J}_{\mathrm{S}}^{\mathrm{MoM}}=2\boldsymbol{n}\times\left(\bar{\nabla}\times\int_{S}\boldsymbol{J}_{\mathrm{S}}^{\mathrm{MoM}}g\,\mathrm{d}S+\boldsymbol{H}^{\mathrm{i}}\right)\quad(\text{in the lit PO region}).\tag{10}$$

We expand the currents using separate sets of basis functions $\boldsymbol{B}_{\mathrm{MoM}}$ and $\boldsymbol{B}_{\mathrm{PO}}$ for the MoM and PO regions, respectively, and test the integral equations using separate testing (weighting) functions $\boldsymbol{T}^{\mathrm{MoM}}$ and $\boldsymbol{T}^{\mathrm{PO}}$ for the two regions. The complete hybrid MoM-PO system matrix equation can then be expressed as [5]

$$\begin{bmatrix}Z_{\mathrm{MoM}}^{\mathrm{MoM}} & Z_{\mathrm{PO}}^{\mathrm{MoM}}\\ P_{\mathrm{MoM}}^{\mathrm{PO}}-Z_{\mathrm{MoM}}^{\mathrm{PO}} & P_{\mathrm{PO}}^{\mathrm{PO}}\end{bmatrix}\cdot\begin{bmatrix}I_{\mathrm{MoM}}\\ I_{\mathrm{PO}}\end{bmatrix}=\begin{bmatrix}V^{\mathrm{MoM}}\\ V^{\mathrm{PO}}\end{bmatrix}.\tag{11}$$

Applying the surface divergence theorem and having in mind that divergence-conforming testing functions on the elements in the MoM region will be used [19], the elements of the MoM-MoM and MoM-PO impedance matrices are obtained as

$$\begin{aligned}z_{\mathrm{MoM/PO}}^{\mathrm{MoM}}=\mathrm{j}\omega\mu&\int_{S^{(\mathrm{t})}}\int_{S^{(\mathrm{b})}}\boldsymbol{T}^{\mathrm{MoM}}\cdot\boldsymbol{B}_{\mathrm{MoM/PO}}g\,\mathrm{d}S^{(\mathrm{b})}\mathrm{d}S^{(\mathrm{t})}\\&-\frac{\mathrm{j}}{\omega\varepsilon}\int_{S^{(\mathrm{t})}}\int_{S^{(\mathrm{b})}}(\nabla_S\cdot\boldsymbol{T}^{\mathrm{MoM}})(\nabla_S\\&\cdot\boldsymbol{B}_{\mathrm{MoM/PO}})g\,\mathrm{d}S^{(\mathrm{b})}\,\mathrm{d}S^{(\mathrm{t})}\end{aligned}\tag{12}$$

("MoM/PO" in the subscripts means "MoM or PO"), while the PO-MoM interaction impedances are given by

$$z_{\mathrm{MoM}}^{\mathrm{PO}}=\int_{S^{(\mathrm{t})}}\boldsymbol{T}^{\mathrm{PO}}\cdot\boldsymbol{n}\times\left[\bar{\nabla}\times\int_{S^{(\mathrm{b})}}\bar{\boldsymbol{B}}_{\mathrm{MoM}}g\,\mathrm{d}S^{(\mathrm{b})}\right]\mathrm{d}S^{(\mathrm{t})}\quad(\text{if in the lit region}).\tag{13}$$

The elements of the PO-MoM and PO-PO projection matrices are

$$p_{\mathrm{MoM/PO}}^{\mathrm{PO}}=\frac{1}{2}\int_{S^{(\mathrm{t})}}\boldsymbol{T}^{\mathrm{PO}}\cdot\boldsymbol{B}_{\mathrm{MoM/PO}}\mathrm{d}S^{(\mathrm{t})}.\tag{14}$$

Finally, the MoM and PO voltages (excitation-matrix elements) are evaluated as

$$v^{\mathrm{MoM}}=\int_{S^{(\mathrm{t})}}\boldsymbol{T}^{\mathrm{MoM}}\cdot\boldsymbol{E}^{\mathrm{i}}\mathrm{d}S^{(\mathrm{t})}\tag{15}$$

$$v^{\mathrm{PO}}=\int_{S^{(\mathrm{t})}}\boldsymbol{T}^{\mathrm{PO}}\cdot(\boldsymbol{n}\times\boldsymbol{H}^{\mathrm{i}})\,\mathrm{d}S^{(\mathrm{t})}.\tag{16}$$

In (12)–(16), $S^{(\mathrm{b})}$ and $S^{(\mathrm{t})}$ represent the domains of basis and testing functions, respectively. Note that the reduced complexity of the MoM-PO method, as compared to the full MoM, is achieved by neglecting the mutual interactions between the PO currents, therefore eliminating from the matrix equation the large, dense, matrix $Z_{\mathrm{PO}}^{\mathrm{PO}}$. From the second equation of the two partitioned matrix equations equivalent to (11), the unknown PO current coefficients I_{PO} can be expressed as

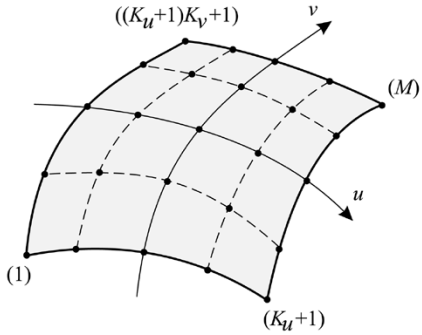

Fig. 2. Generalized curved parametric quadrilateral of arbitrary geometrical orders for modeling of MoM and PO surfaces.

$$I_{\mathrm{PO}}=\left(P_{\mathrm{PO}}^{\mathrm{PO}}\right)^{-1}\left[V^{\mathrm{PO}}-\left(P_{\mathrm{MoM}}^{\mathrm{PO}}-Z_{\mathrm{MoM}}^{\mathrm{PO}}\right)I_{\mathrm{MoM}}\right].\tag{17}$$

Substituting this expression in the first partitioned equation of (11) then leads to the following matrix equation:

$$\begin{aligned}\left[Z_{\mathrm{MoM}}^{\mathrm{MoM}}-Z_{\mathrm{PO}}^{\mathrm{MoM}}\left(P_{\mathrm{PO}}^{\mathrm{PO}}\right)^{-1}\left(P_{\mathrm{MoM}}^{\mathrm{PO}}-Z_{\mathrm{MoM}}^{\mathrm{PO}}\right)\right]I_{\mathrm{MoM}}\\=V^{\mathrm{MoM}}-Z_{\mathrm{PO}}^{\mathrm{MoM}}\left(P_{\mathrm{PO}}^{\mathrm{PO}}\right)^{-1}V^{\mathrm{PO}}\end{aligned}\tag{18}$$

which can be solved for the unknown MoM current coefficients I_{MoM}. Once the MoM currents are known, the PO currents can be obtained using (17).

B. Geometrical Modeling of MoM and PO Surfaces

In this paper, generalized curved parametric quadrilaterals of higher (theoretically arbitrary) geometrical orders [19] are adopted as basic elements for the approximation of all the surfaces in the system, in both the MoM and PO regions. A generalized quadrilateral (Fig. 2) is determined by $M=(K_u+1)(K_v+1)$ points (interpolation nodes) arbitrarily positioned in space, where K_u and K_v $(K_u,K_v\geq 1)$ are geometrical orders of the element along the u- and v- parametric coordinate, respectively. The quadrilateral can be described analytically as

$$\boldsymbol{r}(u,v)=\sum_{i=1}^{M}\boldsymbol{r}_i p_i(u,v)=\sum_{k=0}^{K_u}\sum_{l=0}^{K_v}\boldsymbol{r}_{kl}u^k v^l\quad -1\leq u,v\leq 1\tag{19}$$

where $\boldsymbol{r}_1,\boldsymbol{r}_2,\ldots,\boldsymbol{r}_M$ are the position vectors of the interpolation nodes, $p_i(u,v)$ are Lagrange-type interpolation polynomials satisfying the Kronecker delta relation $p_i(u_j,v_j)=\delta_{ij}$, with u_j and v_j representing the parametric coordinates of the jth node, and $\boldsymbol{r}_{kl}$ are constant vector coefficients related to $\boldsymbol{r}_1,\boldsymbol{r}_2,\ldots,\boldsymbol{r}_M$.

C. Higher Order Basis and Testing Functions in the MoM Region

The surface electric current density vector over quadrilaterals in both the MoM and PO regions is represented as

$$\begin{aligned}\boldsymbol{J}_{\mathrm{S}}(u,v) &= \sum \alpha \boldsymbol{B}(u,v) \\ &= \frac{1}{\left|\frac{\partial \boldsymbol{r}}{\partial u}\times\frac{\partial \boldsymbol{r}}{\partial v}\right|}\left[\sum_{i=0}^{N_u}\sum_{j=0}^{N_v-1}\alpha_{uij}f_{uij}(u,v)\frac{\partial \boldsymbol{r}}{\partial u}\right. \\ &\quad \left. + \sum_{i=0}^{N_u-1}\sum_{j=0}^{N_v}\alpha_{vij}f_{vij}(u,v)\frac{\partial \boldsymbol{r}}{\partial v}\right] \end{aligned} \tag{20}$$

where f are divergence-conforming basis functions of coordinates u and v, N_u and N_v are the adopted orders of the current approximation, α_{uij} and α_{vij} are unknown current-distribution coefficients, and $\boldsymbol{r} = \boldsymbol{r}(u,v)$ is given in (19).

In the MoM region, the following simple divergence-conforming hierarchical polynomials of arbitrary orders [16], [17], [19] are adopted as basis functions

$$f_{\mathrm{MoM},uij}(u,v) = \left\{\begin{array}{cc} u+1, & i=0 \\ u-1, & i=1 \\ u^i-1, & i\geq 2,\mathrm{even} \\ u^i-u, & i\geq 3,\mathrm{odd}\end{array}\right\} v^j \tag{21}$$

with an analogous expression for f^{MoM}_{vij}. The same functions are used for testing, which gives rise to the Galerkin method.

Note that if the MoM subsystem is to be solved by an iterative procedure and the number of unknowns in the MoM region is very large, alternative higher order hierarchical polynomial basis functions with improved orthogonality and conditioning properties [20] may be implemented to accelerate the solution procedure. However, these basis functions, being more complicated than the regular polynomials in (21), require larger MoM matrix filling times, and are therefore impractical when iterative solvers (e.g., those based on the conjugate gradient method) are not used for the MoM part of the system.

Note also that the MoM solution to EFIE (1) using expansions (21) appears to yield equally accurate results at internal resonances of closed metallic surfaces [19], even though the condition number of the MoM matrix is very large at these frequencies (the solution is sensitive to internal resonances only when the current approximation orders are not sufficient).

Wires are modeled using the thin-wire (reduced-kernel) approximation and the 1-D version of the basis functions in (21). Of course, wires (and wire-surface junctions) must belong to the MoM region (the PO does not make sense for wires).

D. Higher Order Basis and Testing Functions in the PO Region

If the basis and testing functions in the PO region are chosen to be the same as in the MoM region, the inverse of the projection matrix $P^{\mathrm{PO}}_{\mathrm{PO}}$ becomes block-diagonal, where each block corresponds to a group of connected quadrilateral surfaces in the PO region. If all of the elements in the PO region form a single, connected PO surface (which is the case most frequently encountered in practical applications), then $(P^{\mathrm{PO}}_{\mathrm{PO}})^{-1}$ is dense,

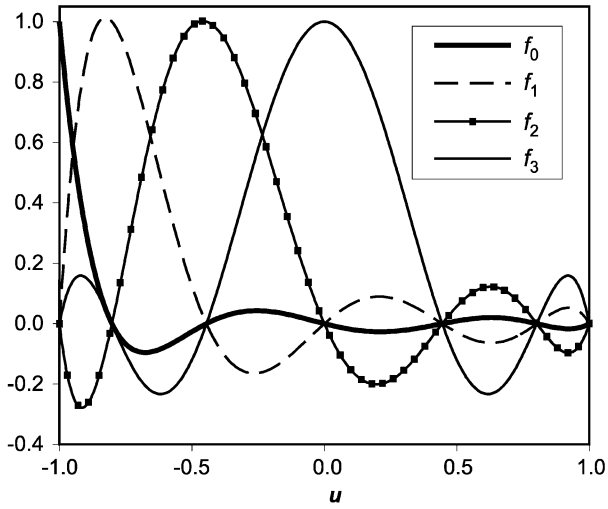

Fig. 3. Representative 1-D sixth-order interpolatory basis functions based on modified Chebyshev polynomials (f_0, f_1, f_2, and f_3 are nonzero for $u = -1, -0.802, -0.445$, and 0, respectively).

and the overall analysis becomes extremely costly in terms of the required memory and computation time.

The computational cost associated with the inversion of the projection matrix $P^{\mathrm{PO}}_{\mathrm{PO}}$ and matrix multiplications in (17) and (18) can be considerably reduced by a proper choice of basis and testing functions in the PO region. If the surface currents in the PO region are expanded in terms of interpolatory polynomials and a modified point-matching technique is applied at the interpolation points, $P^{\mathrm{PO}}_{\mathrm{PO}}$ can be made an identity matrix and (17)–(18) reduced to

$$\begin{aligned}&\left[Z^{\mathrm{MoM}}_{\mathrm{MoM}} - Z^{\mathrm{MoM}}_{\mathrm{PO}}\left(P^{\mathrm{PO}}_{\mathrm{MoM}} - Z^{\mathrm{PO}}_{\mathrm{MoM}}\right)\right] I_{\mathrm{MoM}} \\ &\quad = V^{\mathrm{MoM}} - Z^{\mathrm{MoM}}_{\mathrm{PO}} V^{\mathrm{PO}} \end{aligned} \tag{22}$$

$$I_{\mathrm{PO}} = V^{\mathrm{PO}} - \left(P^{\mathrm{PO}}_{\mathrm{MoM}} - Z^{\mathrm{PO}}_{\mathrm{MoM}}\right) I_{\mathrm{MoM}}. \tag{23}$$

With this aim in mind, we choose 2-D interpolatory polynomials based on modified Chebyshev polynomials as basis functions in the PO region. In specific

$$f_{\mathrm{PO},uij}(u,v) = C_{uij}\frac{\mathcal{T}^{\mathrm{mod}}_{N_u+1}(u)}{u-u^{\mathrm{mod}}_i}\frac{\mathcal{T}_{N_v}(v)}{v-v_j} \tag{24}$$

where $\mathcal{T}^{\mathrm{mod}}_{N_u+1}(u)$ and $\mathcal{T}_{N_v}(v)$ are the modified and regular Chebyshev polynomials, respectively, and C_{uij} is a normalization factor. The zeros of modified polynomials, u^{mod}_i, are obtained by scaling the zeros of regular Chebyshev polynomials by a factor of $\cos\{\pi/[2(N_u+1)]\}$. The left-most and right-most zeros therefore have a value of -1 and $+1$, respectively, making the basis functions divergence conforming on the segment $[-1,1]$. Fig. 3 shows several basis functions based on modified Chebyshev polynomials in one dimension. Note that an interpolation based on polynomials with arbitrary distribution of zeros on the segment $[-1,1]$ could also have been used. Such interpolation, however, would yield basis functions with larger nonmaximum "ripples."

We also note that the use of basis functions (24) in conjunction with the point-matching testing procedure allows junctions

of generalized quadrilaterals with different current-approximation orders. For example, if the nth quadrilateral in the model shares an edge defined by $u_n = -1$ with the mth one, the continuity of the normal surface current density component across the common edge is enforced by adopting the basis functions of the nth quadrilateral that correspond to the common edge in the following form:

$$f_{\mathrm{PO(n)},uij}(u,v) = C_{uij}\frac{\mathcal{T}^{\mathrm{mod}}_{N_u+1}(u)}{u-(-1)}\cdot\frac{\mathcal{T}_{\min(N_{vm},N_{vn})}(v)}{v-v_j}$$
$$j = 0,1,\ldots,\min(N_{vm},N_{vn}) \tag{25}$$

so that the interpolation points of the basis functions along the edge are the same for the two quadrilaterals. The orders of other basis functions on the nth quadrilateral do not depend on the expansions in neighboring elements. This yields the same flexibility in discretizing the PO surfaces using elements of different sizes and shapes (with the corresponding current-approximation orders) as with the use of the hierarchical MoM basis functions (21) [19]. At the external edges of open metallic surfaces, the normal component of $\boldsymbol{B}_{\mathrm{PO}}$ is forced to zero, which means that $\boldsymbol{J}_{\mathrm{S}}^{\mathrm{PO}}$ differs from the conventional PO current in (8) in the vicinity of these edges.

Given the definition of $P_{\mathrm{PO}}^{\mathrm{PO}}$ in (14), we conclude that its reduction to an identity matrix requires that the point-matching testing functions in the PO region, $\boldsymbol{T}^{\mathrm{PO}}$, satisfy the Kronecker relationship

$$\frac{1}{2}\int\limits_{S^{(t)}} \boldsymbol{T}^{\mathrm{PO}}_{(m)}\cdot\boldsymbol{B}_{\mathrm{PO}(n)}\,\mathrm{d}S^{(t)} = \delta_{mn} = \begin{cases}1, & m=n\\ 0, & m\neq n.\end{cases} \tag{26}$$

The testing functions defined on higher order quadrilaterals have the following general form:

$$\boldsymbol{T}^{\mathrm{PO}}_{(m)}(u,v) = \frac{1}{\left|\frac{\partial\boldsymbol{r}}{\partial u}\times\frac{\partial\boldsymbol{r}}{\partial v}\right|}\boldsymbol{t}_m(u,v)\delta(u-u_m,v-v_m) \tag{27}$$

which reduces (26) to

$$\frac{1}{2}\boldsymbol{t}_m(u_m,v_m)\cdot\boldsymbol{B}_{\mathrm{PO}(n)}(u_m,v_m) = \delta_{mn}. \tag{28}$$

The point matching technique is performed exactly at the interpolation points of the basis functions, and hence

$$\boldsymbol{B}_{\mathrm{PO}(n)}(u_m,v_m) = 0 \quad (\text{if } m\neq n). \tag{29}$$

To construct the testing function that corresponds to the u-directed basis function, we note that, at the interpolation point (u_m,v_m), only one u-directed and almost all v-directed basis functions are nonzero. Therefore, the corresponding testing function has to be constructed in such a manner that its product with current expansion functions equals one for u-directed basis function and zero for v-directed basis functions. Accordingly, the testing function is chosen to be perpendicular to the v parametric coordinate

$$\boldsymbol{t}_m(u_m,v_m) = t_m(u_m,v_m)\hat{w}, \tag{30}$$

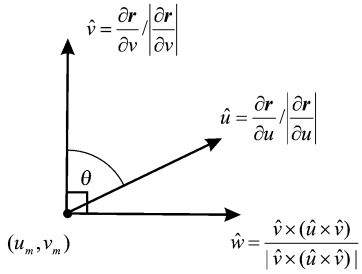

Fig. 4. Surface unit vectors $\hat{u}$ and $\hat{v}$ along the two parametric coordinates and unit vector $\hat{w}$ of the testing function corresponding to the u-directed basis function (all vectors are in the same plane).

where $\hat{w}$ is the unit vector perpendicular to $\hat{v}(\hat{w}\cdot\hat{v}=0)$ at the point (u_m,v_m) (Fig. 4)

$$\hat{w} = \left[\frac{\hat{v}\times(\hat{u}\times\hat{v})}{|\hat{v}\times(\hat{u}\times\hat{v})|}\right]_{\substack{u=u_m\\v=v_m}} = \left[\frac{\hat{v}\times(\hat{u}\times\hat{v})}{\sin\theta}\right]_{\substack{u=u_m\\v=v_m}} \tag{31}$$

θ being the angle between the unit vectors $\hat{u}$ and $\hat{v}$ along the parametric coordinates. The dot product of testing and basis functions can, therefore, be expressed as

$$\begin{aligned}&\boldsymbol{t}_m(u_m,v_m)\cdot\boldsymbol{B}_{\mathrm{PO}(n)}(u_m,v_m)\\ &\quad= t_m(u_m,v_m)\frac{1}{\left|\frac{\partial\boldsymbol{r}}{\partial u}\times\frac{\partial\boldsymbol{r}}{\partial v}\right|_{\substack{u=u_m\\v=v_m}}}f_{\mathrm{PO(n)}}(u_m,v_m)\hat{w}\\ &\qquad\cdot\left.\frac{\partial\boldsymbol{r}}{\partial u}\right|_{\substack{u=u_m\\v=v_m}}\cdot\\ &\quad= t_m(u_m,v_m)\frac{1}{\left|\frac{\partial\boldsymbol{r}}{\partial v}\right|_{\substack{u=u_m\\v=v_m}}}f_{\mathrm{PO(n)}}(u_m,v_m).\end{aligned} \tag{32}$$

Since $f(u_m,v_m)=1$, we conclude that a choice

$$\boldsymbol{t}_m(u_m,v_m) = 2\left|\frac{\partial\boldsymbol{r}}{\partial v}\right|_{\substack{u=u_m\\v=v_m}}\hat{w} \tag{33}$$

ensures that $P_{\mathrm{PO}}^{\mathrm{PO}}$ is an identity matrix, which gives rise to the following final expression for the testing function corresponding to the u-directed basis function in the PO region

$$\boldsymbol{T}^{\mathrm{PO}}_{(m)}(u,v) = \frac{2}{\left|\frac{\partial\boldsymbol{r}}{\partial u}\times\frac{\partial\boldsymbol{r}}{\partial v}\right|}\left|\frac{\partial\boldsymbol{r}}{\partial v}\right|_{\substack{u=u_m\\v=v_m}}\delta(u-u_m,v-v_m)\hat{w}. \tag{34}$$

The testing function that corresponds to the v-directed basis function is constructed in an analogous manner.

In general, regardless of the particular choices of basis and testing functions proposed and implemented in this paper, it is worth noting that it is impossible to implement the Galerkin testing in conjunction with the current continuity (divergence conformity) of basis sets in the PO region and still have the projection matrix $P_{\mathrm{PO}}^{\mathrm{PO}}$ be an identity matrix. These features are contradictory because the orthogonality condition (26) requires that all of the zeros of all of the expansion functions over PO elements belong to the interior of the element, while the current-continuity condition requires that some of the higher order functions have some of their zeros at the element edges, i.e., at the boundaries of integration domains. While it is extremely

important to ensure the current continuity across the boundaries between the PO elements, the point-matching testing in the PO region, as implemented in this paper, has proved to be accurate enough in all applications and is faster than the Galerkin procedure.

Finally, note that the matrix product $Z_{\rm PO}^{\rm MoM}(P_{\rm MoM}^{\rm PO}-Z_{\rm MoM}^{\rm PO})$ in (22), which becomes very time-consuming when the number of unknowns in the MoM region is large, can be avoided by applying the multiple-reflection iterative approach [5], [11], [13] given by

$$\begin{aligned} Z_{\rm MoM}^{\rm MoM} I_{\rm MoM}^{(N)} &= V^{\rm MoM} - Z_{\rm PO}^{\rm MoM} I_{\rm PO}^{(N-1)} \\ I_{\rm PO}^{(N)} &= V^{\rm PO} - \left(P_{\rm MoM}^{\rm PO} - Z_{\rm MoM}^{\rm PO}\right) I_{\rm MoM}^{(N)} \\ N &= 1,2,\ldots, \quad \text{with } I_{\rm PO}^{(0)} = 0 \end{aligned} \tag{35}$$

instead of the direct solution of (11) using (22) and (23).

E. MoM-PO Interaction Impedance and Projection Matrices for Higher Order Quadrilateral Elements

In this section, we finalize the expressions for the MoM-PO system matrix elements based on proposed higher order basis and testing functions for the MoM and PO regions of a general structure. Without the loss of generality, we consider only the u-components of basis and testing functions. Furthermore, for the basis functions in both the MoM and PO regions and the testing functions in the MoM region (which are the same as the corresponding basis functions), we consider the functions in the following simplified form:

$$\boldsymbol{B}_{ij}(u,v) = \frac{1}{\left|\frac{\partial \boldsymbol{r}}{\partial u}\times\frac{\partial \boldsymbol{r}}{\partial v}\right|}\Gamma_{ij}(u,v)\frac{\partial \boldsymbol{r}(u,v)}{\partial u} \tag{36}$$

where Γ are the simple 2-D power functions

$$\Gamma_{ij}(u,v) = u^i v^j. \tag{37}$$

The impedances and projections corresponding to the complete basis functions defined by (20), (21), and (24) can be obtained as a linear combination of those corresponding to the simplified functions in (36) and (37). Finally, for the matrix elements associated with the basis functions in the MoM region and testing functions in the PO region, we assume that the PO quadrilaterals are not in the shadowed region. If the testing (matching) point is in the shadow, the corresponding matrix elements are zero.

Combining (12), (20), (36), and (37), the impedances for the testing function defined by indices i_m and j_m on the mth quadrilateral in the MoM region and the basis function defined by indices i_n and j_n on the nth quadrilateral in either the MoM or PO region are obtained as

$$\begin{aligned} z_{\rm MoM/PO}^{\rm MoM} &= {\rm j}\omega\mu \int_{u_{1m}}^{u_{2m}}\int_{v_{1m}}^{v_{2m}}\int_{u_{1n}}^{u_{2n}}\int_{v_{1n}}^{v_{2n}} \left(\Gamma_{i_m j_m}\frac{\partial \boldsymbol{r}_m}{\partial u_m}\right)\left(\Gamma_{i_n j_n}\frac{\partial \boldsymbol{r}_n}{\partial u_n}\right) \\ &\quad \times g(R)\,{\rm d}u_n\,{\rm d}v_n\,{\rm d}u_m\,{\rm d}v_m \\ &\quad - \frac{\rm j}{\omega\varepsilon}\int_{u_{1m}}^{u_{2m}}\int_{v_{1m}}^{v_{2m}}\int_{u_{1n}}^{u_{2n}}\int_{v_{1n}}^{v_{2n}} \frac{\partial \Gamma_{i_m j_m}}{\partial u_m}\frac{\partial \Gamma_{i_n j_n}}{\partial u_n} \\ &\quad \times g(R){\rm d}u_n\,{\rm d}v_n\,{\rm d}u_m\,{\rm d}v_m \\ &= \sum_{k_m=1}^{K_u^{(m)}}\sum_{l_m=0}^{K_v^{(m)}}\sum_{k_n=1}^{K_u^{(n)}}\sum_{l_n=0}^{K_v^{(n)}} k_m k_n \boldsymbol{r}_{kl}^{(m)}\cdot\boldsymbol{r}_{kl}^{(n)} \\ &\quad \times \xi(i_m+k_m-1, j_m+l_m, i_n+k_n-1, j_n+l_n) \\ &\quad - \frac{1}{\omega^2\mu\varepsilon} i_m i_n \xi(i_m-1, j_m, i_n-1, j_n) \\ &\qquad i_m = 0,1,\ldots,N_u^{(m)}, \quad j_m = 0,1,\ldots,N_v^{(m)} \\ &\qquad i_n = 0,1,\ldots,N_u^{(n)}, \quad j_n = 0,1,\ldots,N_v^{(n)} \end{aligned} \tag{38}$$

where $(N_u^{(m)}, N_v^{(m)})$ and $(K_u^{(m)}, K_v^{(m)})$ are the current-approximation orders and geometrical orders, respectively, of the mth quadrilateral along the u- and v-coordinate, and $\boldsymbol{r}_{kl}^{(m)}$ are the geometrical vector coefficients in the polynomial expansion of the mth quadrilateral, while $(N_u^{(n)}, N_v^{(n)}), (K_u^{(n)}, K_v^{(n)})$, and $\boldsymbol{r}_{kl}^{(n)}$ are the corresponding parameters for the nth quadrilateral in the model. The integration limits in both quadrilaterals are $u_1 = v_1 = -1$ and $u_2 = v_2 = 1$, and

$$\xi(i_m, j_m, i_n, j_n) = {\rm j}\omega\mu \int_{-1}^{1}\int_{-1}^{1}\int_{-1}^{1}\int_{-1}^{1} u_m^{i_m} v_m^{j_m} u_n^{i_n} v_n^{j_n} g(R)\,{\rm d}u_n\,{\rm d}v_n\,{\rm d}u_m\,{\rm d}v_m. \tag{39}$$

The expressions for the MoM-PO matrix elements that correspond to testing functions in the PO region are considered next. From (13) and (34), the elements of the impedance matrix $Z_{\rm MoM}^{\rm PO}$ have the form

$$\begin{aligned} z_{\rm MoM}^{\rm PO} &= 2\left|\frac{\partial \boldsymbol{r}}{\partial v}\right|_{\substack{u=u_m\\v=v_m}} \hat{w}\cdot\left[\boldsymbol{n}\times\bar{\boldsymbol{H}}(\boldsymbol{B}_{\rm MoM})\right]_{\substack{u=u_m\\v=v_m}} \\ &= 2\left|\frac{\partial \boldsymbol{r}}{\partial v}\right|_{\substack{u=u_m\\v=v_m}} \left(\hat{w}\times\boldsymbol{n}_{\substack{u=u_m\\v=v_m}}\right)\cdot\bar{\boldsymbol{H}}(\boldsymbol{B}_{\rm MoM})_{\substack{u=u_m\\v=v_m}}. \end{aligned} \tag{40}$$

Noting that $\hat{w}\times\boldsymbol{n}_{\substack{u=u_m\\v=v_m}} = -\hat{v}\big|_{\substack{u=u_m\\v=v_m}}$ and using the identity $\nabla\times(\mathbf{C}g) = -\mathbf{C}\times\nabla g$, we can write

$$\begin{aligned} z_{\rm MoM}^{\rm PO} &= -2\left|\frac{\partial \boldsymbol{r}}{\partial v}\right|_{\substack{u=u_m\\v=v_m}} \hat{v}\big|_{\substack{u=u_m\\v=v_m}}\cdot\bar{\nabla}\times\int_{S^{(\rm b)}}\boldsymbol{B}_{\rm MoM} g\,{\rm d}S^{(\rm b)} \\ &= -2\left|\frac{\partial \boldsymbol{r}}{\partial v}\right|_{\substack{u=u_m\\v=v_m}} \int_{S^{(\rm b)}}\left(\boldsymbol{B}_{\rm MoM}\times\hat{v}\big|_{\substack{u=u_m\\v=v_m}}\right)\cdot\bar{\nabla}g\,{\rm d}S^{(\rm b)} \\ &\qquad \text{(for lit region)}. \end{aligned} \tag{41}$$

If the MoM and PO regions overlap and the testing and source surface elements are the same $(m=n)$, $\bar{\nabla}g$ is computed as the average value of ∇g at the two points placed at the same small distance on opposite sides of the surface

$$\begin{aligned} \bar{\nabla}g = \frac{1}{2}\Bigg[&(\boldsymbol{r}_{\rm test}+\boldsymbol{d}-\boldsymbol{r}_{\rm source})\frac{1}{R^+}\frac{{\rm d}g(R^+)}{{\rm d}R^+} \\ &+(\boldsymbol{r}_{\rm test}-\boldsymbol{d}-\boldsymbol{r}_{\rm source})\frac{1}{R^-}\frac{{\rm d}g(R^-)}{{\rm d}R^-}\Bigg] \end{aligned} \tag{42}$$

where $R^{\pm} = |\boldsymbol{r}_{\rm test}\pm\boldsymbol{d}-\boldsymbol{r}_{\rm source}|$ and $\boldsymbol{d} = \boldsymbol{n}d$ is the displacement vector perpendicular to the surface at the testing point, with the displacement d being very small when compared to the quadrilateral dimensions. When the testing and source points

coincide ($\boldsymbol{r}_{\rm test} = \boldsymbol{r}_{\rm source}$), $R^{\pm} = d$. When they are close to each other, the vector $\boldsymbol{r}_{\rm test} - \boldsymbol{r}_{\rm source}$ is tangential to the surface, and therefore $R^{\pm} \approx \sqrt{|\boldsymbol{r}_{\rm test} - \boldsymbol{r}_{\rm source}|^2 + |\boldsymbol{d}|^2}$. Finally, when the distance between the testing and source points is large compared to d, $R^{\pm} \approx |\boldsymbol{r}_{\rm test} - \boldsymbol{r}_{\rm source}|$. Hence, in all cases we can assume that $R^{+} \approx R^{-}$, so that (42) becomes

$$\bar{\nabla} g \approx (\boldsymbol{r}_{\rm test} - \boldsymbol{r}_{\rm source}) \frac{1}{R^{+}} \frac{{\rm d}g(R^{+})}{{\rm d}R^{+}}. \tag{43}$$

If the testing and source surface elements are not the same, $\bar{\nabla} g = \nabla g$.

With (20), (36), (37), and (43), the final expression for the elements of $Z_{\rm MoM}^{\rm PO}$ is

$$\begin{aligned} z_{\rm MoM}^{\rm PO} &= -2 \left| \frac{\partial \boldsymbol{r}}{\partial v} \right|_{\substack{u=u_m \\ v=v_m}} \int_{u_{1n}}^{u_{2n}} \int_{v_{1n}}^{v_{2n}} \\ &\quad \times \Gamma_{i_n j_n} \left(\frac{\partial \boldsymbol{r}_n}{\partial u_n} \times \hat{v}|_{\substack{u=u_m \\ v=v_m}} \right) \cdot (\boldsymbol{r}_m - \boldsymbol{r}_n) \\ &\quad \times \frac{1}{R} \frac{{\rm d}g(R)}{{\rm d}R} {\rm d}u_n {\rm d}v_n \\ &= 2 \left| \frac{\partial \boldsymbol{r}}{\partial v} \right|_{\substack{u=u_m \\ v=v_m}} \hat{v}|_{\substack{u=u_m \\ v=v_m}} \\ &\quad \cdot \sum_{k_{n1}=0}^{K_u^{(n)}} \sum_{l_{n1}=0}^{K_v^{(n)}} \sum_{k_n=1}^{K_u^{(n)}} \sum_{l_n=0}^{K_v^{(n)}} k_n \left(\boldsymbol{r}_{kl}^{(n)} \times \boldsymbol{r}_{kl}^{(n1)*} \right) \\ &\quad \times \psi(i_n + k_n + k_{n1} - 1, j_n + l_n + l_{n1}) \end{aligned} \tag{44}$$

where

$$\boldsymbol{r}_{kl}^{(n1)*} = \begin{cases} \boldsymbol{r}_{kl}^{(n1)} - \boldsymbol{r}_m & k = 0, \quad l = 0 \\ \boldsymbol{r}_{kl}^{(n1)} & \text{otherwise} \end{cases} \tag{45}$$

and

$$\psi(i_n, j_n) = \int_{u_{1n}}^{u_{2n}} \int_{v_{1n}}^{v_{2n}} u_n^{i_n} v_n^{j_n} \frac{1}{R} \frac{{\rm d}g(R)}{{\rm d}R} {\rm d}u_n {\rm d}v_n. \tag{46}$$

For the testing quadrilateral coinciding with the source one, R is to be substituted by R^{+} in (44) and (46) according to (43), i.e., the integrals are computed slightly above the quadrilateral surface. Based on extensive numerical experiments, we have found that the concrete value of the small displacement d above the surface is not critical at all for the accuracy of the results, and have adopted a value of 10^{-5} times the maximum dimension (diagonal) of the quadrilateral for this parameter in the MoM-PO code.

Rapid and accurate recursive procedures for evaluation of MoM-PO impedances in (38) and (44) are developed, which ensure that the CPU time per unknown in higher order, large-domain solutions is comparable to that in low-order, small-domain solutions. Similar procedures for evaluation of MoM impedances in the case of volume-integral-equation analysis of dielectric scatterers are explained in [21]. When the testing (field) point is close to or lies in the source quadrilateral surface, the integrals (39) and (46) are solved by combined analytical/numerical integration procedures that include the (quasi)singularity extraction [21].

For an arbitrary structure modeled by a system of generalized curvilinear quadrilaterals, a testing point in the PO region can be in the shadow with respect to one part of the source quadrilateral, while being lit by the remainder of the quadrilateral. Therefore, the exact implementation of the shadow condition (8) at this point implies the integration [in (46)] of the associated basis functions only over the part of the source quadrilateral that is actually visible from the testing point. This, in turn, means that the shadow/lit determination must be carried out for all pairs of testing points (in the PO region) and numerical-integration points (in the MoM region), which in some cases is exceedingly time consuming. The cost of multiple shadow determinations can be reduced if the "point-to-point" approach is applied in combination with the "element-to-point" and "element-to-element" approaches so that the overall computation time is minimized without sacrificing accuracy. The development of an optimal solution to the visible surface determination problem for a general geometry, which itself is a challenging research task (similar problems are encountered in computer graphics applications), and its adaptive implementation combining the above three "source-to-target" ray-tracing approaches is part of our current and future work.

The projection matrix $P_{\rm MoM}^{\rm PO}$ is nonzero only if there is an overlapping between the MoM and PO current-domains. For example, such overlapping occurs for currents of the zeroth and first approximation orders [which serve for adjusting the current-continuity boundary condition at the corresponding quadrilateral edges ($u, v = \pm 1$)] in quadrilaterals that share an edge belonging to the boundary between the MoM and PO regions. Although the associated zeroth- and first-order functions $\boldsymbol{B}_{\rm MoM}$ are defined on generalized quadrilaterals that are geometrically on the PO surfaces, computationally they belong to the MoM current-domain in order to enable the automatic adjustment of the current-continuity condition across the boundary. Using (14), (34), and (36), the elements of $P_{\rm MoM}^{\rm PO}$, if nonzero, are evaluated as

$$\begin{aligned} p_{\rm MoM}^{\rm PO} &= \frac{1}{2} 2 \left| \frac{\partial \boldsymbol{r}}{\partial v} \right|_{\substack{u=u_m \\ v=v_m}} \frac{1}{\left| \frac{\partial \boldsymbol{r}}{\partial u} \times \frac{\partial \boldsymbol{r}}{\partial v} \right|_{\substack{u=u_m \\ v=v_m}}} \Gamma_{ij}(u_m, v_m) \hat{w} \\ &\quad \cdot \left. \frac{\partial \boldsymbol{r}}{\partial u} \right|_{\substack{u=u_m \\ v=v_m}} = \Gamma_{ij}(u_m, v_m). \end{aligned} \tag{47}$$

Although the matrix $P_{\rm MoM}^{\rm PO}$ is not an identity matrix, this does not add significantly to the complexity of the method and computation cost of the analysis, because $P_{\rm MoM}^{\rm PO}$ is added to the negative of the dense impedance matrix $Z_{\rm MoM}^{\rm PO}$ in (22)–(23) or (35), and no additional matrix inversion or multiplication is needed.

The projection matrix $P_{\rm PO}^{\rm PO}$ is an identity matrix and does not appear in (22)–(23) and (35).

Finally, note that the MFIE (2) and the PO approximation in (8) are formally valid only on smooth surfaces. If the PO region contains sharp edges, the normal $\boldsymbol{n}$ at the testing points belonging to these edges is not defined. In such cases, $\boldsymbol{n}$ is determined similarly as in [8], as the average of the corresponding normal vectors on the two connected surfaces, that is, on the two adjacent quadrilateral elements, at points close to the boundary.

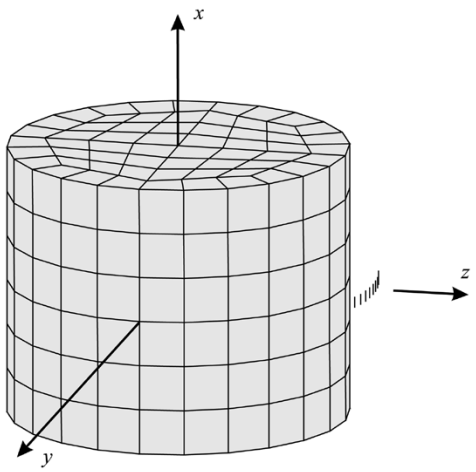

Fig. 5. Simulated higher order MoM-PO geometrical model of an antenna system consisting of an array of nine $\lambda/2$ dipoles in front of a large metallic cylinder of finite length (all dipoles are fed by generators of equal amplitudes and phases).

III. Numerical Results and Discussion

We present three characteristic realistic examples aimed at demonstrating the accuracy and efficiency of the proposed higher order MoM-PO technique. All the simulations are performed on a relatively modest PC (AMD XP-1700+ with 512 MB of RAM).

A. Array of Dipoles in Front of a Large Metallic Cylinder

As the first example, consider an antenna system consisting of an array of nine $\lambda/2$ dipoles in front of a circular metallic cylinder (Fig. 5). The diameter of the cylinder is 15λ and its height 12λ. The wire diameter for the dipoles is $\lambda/1000$. The dipoles are parallel to the cylinder axis and are situated 1.25λ from the cylinder surface with an angular separation of 3.75° between the adjacent dipoles in the array. All of the dipoles are center-fed by point generators of equal amplitudes and phases. The lateral surface (barrel) of the cylinder is approximated using 144 quadrilaterals of the second geometrical orders ($K_u = K_v = 2$) and each of the cylinder bases (caps) is represented by a total of 24 second-order and 36 first-order ($K_u = K_v = 1$) geometrical elements, with the seventh-order current approximation in both parametric coordinates ($N_u = N_v = 7$) for all of the quadrilaterals in the model. All quadrilaterals are approximately 2λ on a side, which is 20 times the usual low-order limit of $\lambda/10$. Each dipole is modeled using two straight wire segments with fourth-order current approximations ($N_u = 4$). In the hybrid MoM-PO analysis, the dipole array is in the MoM region and the cylinder is in the PO region. Note that the shadow condition (8) is enforced in this example for individual dipoles independently at all matching points in the PO region, that is, the lit and shadow regions of the cylinder depend on the source location in the MoM region.

Fig. 6 shows the computed radiation pattern of the array in three characteristic planes that contain the z-axis and form an angle of (a) 0°, (b) 45°, and (c) 90°, respectively, with the central dipole of the array. In all of the cuts, we observe an excellent agreement of the results obtained by the hybrid MoM-PO method and the full MoM results in the front region (for angles

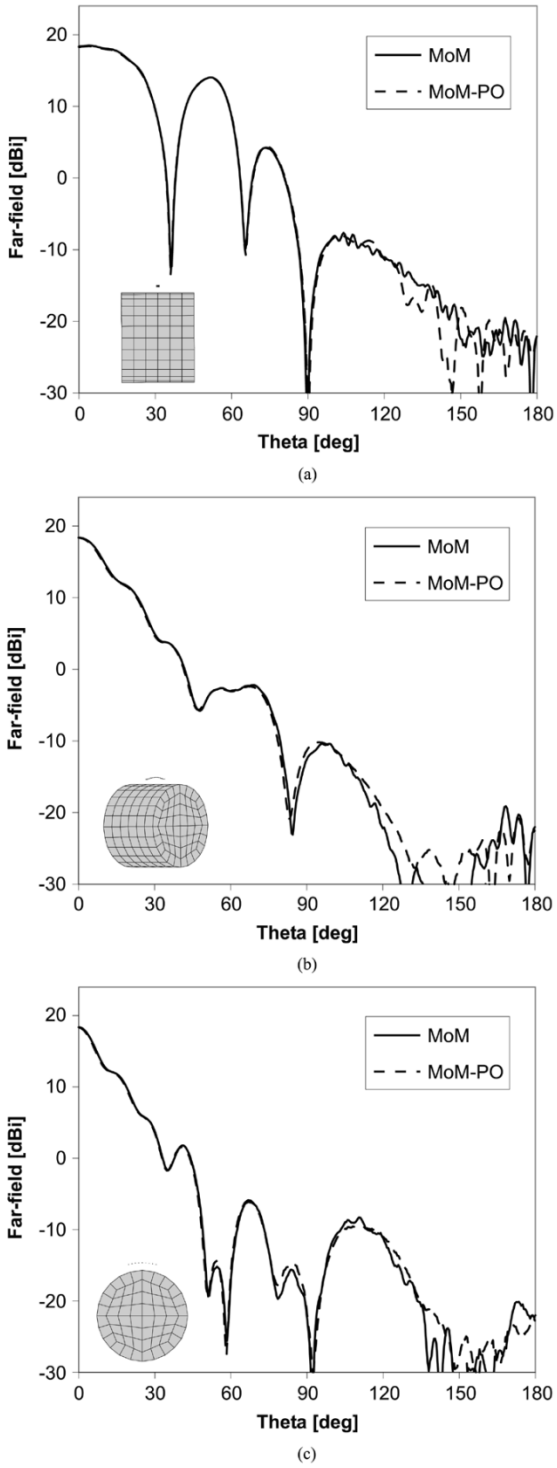

Fig. 6. Far field of the antenna system in Fig. 5, computed by the full MoM and hybrid MoM-PO higher order techniques, respectively, in planes defined by (a) $\phi = 0°$, (b) $\phi = 45°$, and (c) $\phi = 90°$ (ϕ is the standard cylindrical angle measured from the positive x-axis around the z-axis in Fig. 5).

up to 90°) with the largest difference (of approximately 1 dB) being in the cuts (b) and (c) for the angle of about 85°. In the back region (for angles between 90° and 180°), however, the MoM-PO prediction is not accurate enough. The discrepancy between the pure MoM and hybrid MoM-PO here is certainly primarily due to the fact that the currents over the parts of the cylinder surface in the shadow region (it includes both caps and

a large portion of the cylinder barrel), which are quite weak as compared to the currents in the lit region but contribute significantly to the (low-field) radiation in the back region of the antenna system, are set to be zero [(8)] in the MoM-PO simulation.

Using the two-fold symmetry of the problem, the total number of unknowns for the antenna system amounts to 6181 with both techniques. In the pure MoM analysis, the portion of the overall CPU time needed for the matrix filling and that for the solution of the system of linear equations by LU decomposition are 226 and 907 s, respectively. In the hybrid MoM-PO analysis, the number of unknowns in the MoM region is 20 and that in the PO region 6461. The CPU times for filling the MoM-PO matrices and solving the system of equations are 1.9 and 0.03 s, respectively, which is by three orders of magnitude faster than with the rigorous (full MoM) higher order technique. Note also that the estimated number of unknowns, based on a topological analysis, for a common low-order small-domain MoM-PO solution with RWG basis functions on triangular patches and the use of two-fold symmetry is more than 65 000 for the analysis of the same problem.

B. Monopole Antenna Attached to a Large Square Metallic Plate

Consider next a vertical $\lambda/4$ monopole antenna attached at the center of a horizontal metallic square plate 9λ on a side. The monopole is modeled using a single straight wire segment with the third-order current approximation $(N_u = 3)$. The wire diameter equals $\lambda/1000$. The plate is represented by a total of 84 quadrilaterals of the first geometrical orders $(K_u = K_v = 1)$, as shown in Fig. 7. This model consists of 80 square patches (each λ on a side) with the fifth-order current approximation in both parametric coordinates and four trapezoidal (triangle-like) quadrilaterals around the wire-to-surface junction with the third- and fourth-order current approximations in different directions. The triangle-like surface elements enable current continuity across the junction without introducing special junction basis functions. The structure is analyzed using the pure MoM and two hybrid MoM-PO models. In the first MoM-PO arrangement, the MoM region consists of the monopole and the four triangle-like patches in the junction, while all of the square patches are in the PO region, as indicated in Fig. 7(a). The second MoM-PO arrangement, shown in Fig. 7(b), introduces an additional layer (rim) of MoM surface elements along the plate edges, to improve the hybrid solution. Note that the MoM-PO model (b) contains junctions of MoM and PO elements both around the triangle-like MoM elements in the wire-to-surface junction and along the square-shaped MoM elements near the plate edges. Note also that the basis functions on the PO elements in these MoM-PO junctions that serve for adjusting the current-continuity condition for the normal component of $\boldsymbol{J}_{\mathrm{S}}$ along an edge shared with a MoM element are actually treated as MoM basis functions and computationally belong to the MoM current-domain.

Fig. 8 shows the dominant component of the surface current density vector induced on the plate along the line connecting the center of the plate (monopole junction) and the center of one of its sides. As can be seen, while the magnitude and phase of the current density predicted by both hybrid models agree

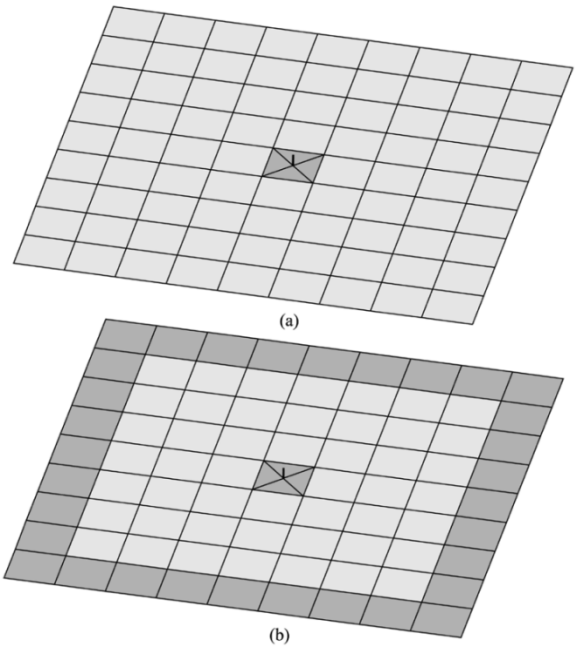

Fig. 7. Hybrid MoM-PO models of a metallic square plate with an attached monopole antenna at the plate center consisting of (a) 5 MoM and 80 PO elements and (b) 37 MoM and 48 PO elements (MoM and PO patches are shaded dark gray and light gray, respectively).

well with the pure MoM solution over the interior part of the plate surface, the improved hybrid model with the MoM rim in Fig. 7(b) yields much better prediction for the current behavior near the plate edge than the model in Fig. 7(a). Note that the currents in the MoM region of both MoM-PO models almost exactly overlap with the corresponding parts of the full MoM solution. Note also that the numerical values constituting the MoM-PO current density curves indicate slight (almost invisible) mismatches in the slope (first derivative) of the curves at the boundaries between MoM and PO regions in the models [for the model in Fig. 7(b), they are located 0.5λ and 3.5λ from the plate center]. This can be attributed to the fact that the current distribution coefficients corresponding to those basis functions that are zero at the MoM-PO boundary and do not influence the value of the current density at the connection, but do contribute to the value of the slope of the current density at the connection, are taken into the overall hybrid system of equations differently at the two sides of the boundary. On the MoM side, they are expressed numerically exactly from the EFIE, while the PO approximation of the MFIE is employed on the PO side of the junction.

The antenna impedance computed in both MoM-PO arrangements, $Z_{\mathrm{MoM-PO(a)}} = (41.30\text{–}\mathrm{j}22.31)\ \Omega$ and $Z_{\mathrm{MoM-PO(b)}} = (41.31\text{–}\mathrm{j}22.31)\ \Omega$, agrees very well with the pure MoM result, $Z_{\mathrm{MoM}} = (41.53\text{–}\mathrm{j}22.63)\ \Omega$.

Shown in Fig. 9 are the far field patterns in two characteristic planes obtained by the three higher order models. We observe that even the first set of hybrid MoM-PO results agrees well with the rigorous MoM solution for both cuts in the upper half-space and in the part of the lower half-space closer to the plane of the plate, with an excellent agreement for angles between 60° and 100° and some inaccuracy for observation points closer to

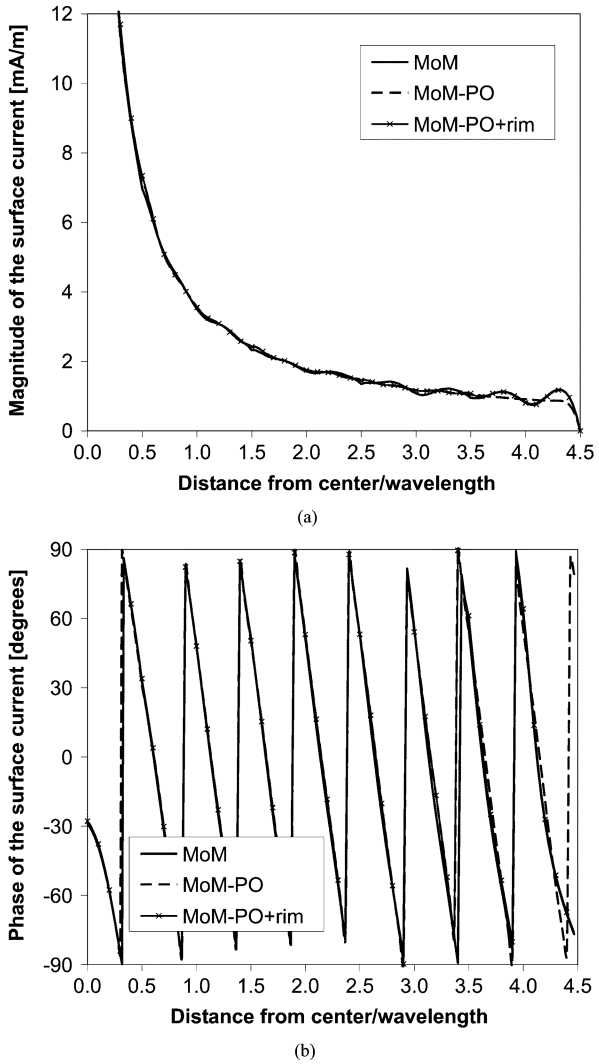

Fig. 8. Magnitude (a) and phase (b) of the surface current density along the line connecting the center (wire junction) and an edge of the plate in Fig. 7 obtained by the full MoM and two hybrid MoM-PO higher order models.

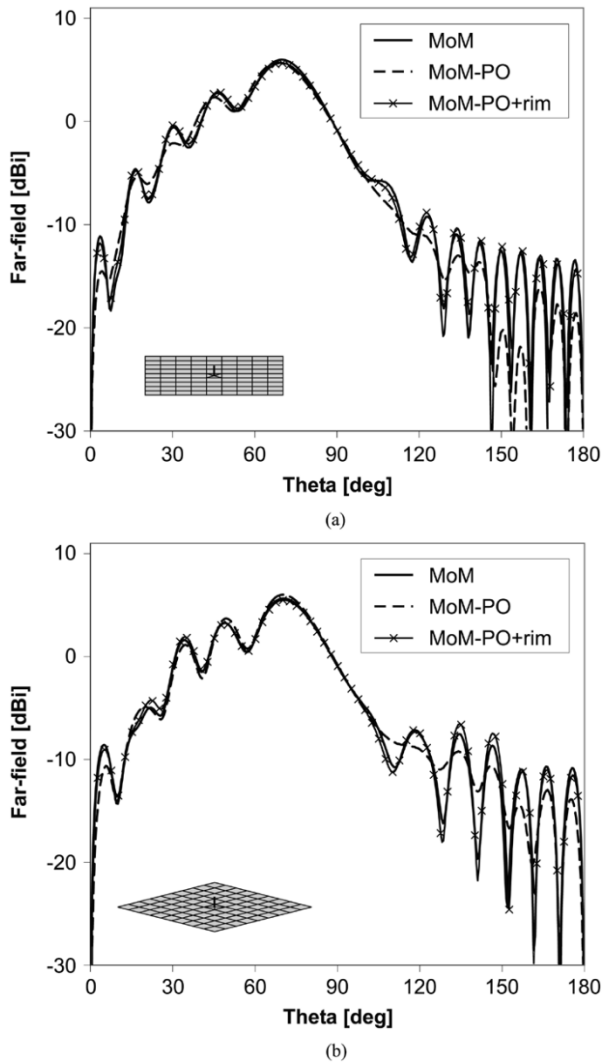

Fig. 9. Far field patterns of the monopole antenna in Fig. 7 obtained using the full MoM and two hybrid MoM-PO higher order models in (a) the plane parallel to a pair of plate edges and (b) the plane containing a plate diagonal.

the monopole axis. However, substantial disagreements of the results using the model in Fig. 7(a) and the full MoM are observed in the shadow region below the plate. On the other hand, the improved arrangement with the MoM rim in Fig. 7(b) yields accurate results in the entire range of angles in both far-field cuts. In particular, the agreement with the full MoM solution is almost perfect in the entire upper half-space and in the deep shadow region, whereas the maximum discrepancies between the two sets of results for the angles between 115° and 150° in the cut (a) and for angles between 100° and 150° in the cut (b) are less than 2 and 3 dB, respectively.

Without the use of symmetry, the total number of unknowns is 4026 in all three higher order arrangements. In the pure MoM approach, the CPU times for filling and solving the system matrix are 21 and 187 s, respectively. The first hybrid MoM-PO arrangement requires 126 MoM and 3900 PO unknowns, and the MoM-PO system filling and solving times are 5.5 and 0.6 s, respectively. With the second MoM-PO arrangement, the distribution of unknowns in the MoM and PO region is 1706 versus 2320, respectively, and the system matrix filling time is 32.5 s. The iterative solution for MoM and PO current coefficients given by (35) is carried out in this case, and the CPU time required is only 2.2 s using 10 multiple-reflection iterations. Note that the simulation of the structure in Fig. 7 using RWG basis functions on small triangular patches would require more than 24 000 unknowns.

C. Parabolic Reflector Antenna With a Pyramidal Horn Feed

The last example is a 14-GHz parabolic reflector antenna system shown in Fig. 10. The reflector is fed by a pyramidal horn, with the phase center of the horn being at the focal point of the reflector. The cross-sectional dimensions of the waveguide feeding the horn are 1.58 cm × 0.79 cm (*Ku*-band waveguide), the horn flare aperture dimensions are 2.52 cm × 2.28 cm, and the lengths of the waveguide and the flare are 3.14 cm and 5 cm, respectively. The entire horn is modeled by 28 flat quadrilaterals of the first geometrical order $(K_u = K_v = 1)$ and of rectangular or trapezoidal shapes, with current approximation orders N_u and N_v ranging from 2 to 8 for different patches. The waveguide is excited by a wire probe in the form of a short dipole modeled by two straight wire segments with the first-order current approximation $(N_u = 1)$. The diameter of the parabolic

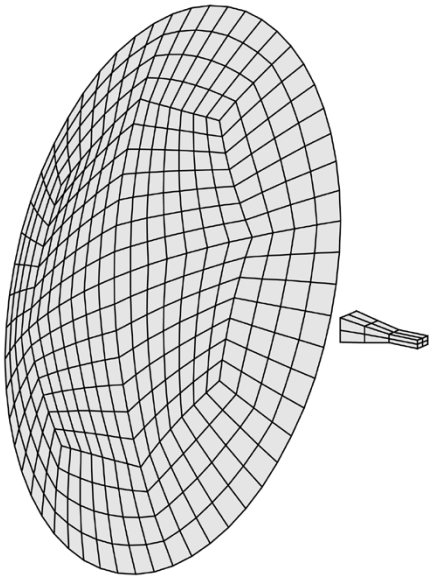

Fig. 10. Simulated higher order MoM-PO geometrical model of a parabolic reflector antenna with a pyramidal horn feed (the horn is excited by a wire probe).

reflector is 51.44 cm and its focal length is 25.72 cm. The reflector surface is modeled using 420 curved quadrilaterals of the second geometrical order $(K_u = K_v = 2)$ with the fifth-order current approximation $(N_u = N_v = 5)$ for all of the quadrilaterals. Note that the surface elements in this model are between 0.88λ and 1.11λ on a side, which is about 10 times the usual small-domain limit. The horn far field pattern is slightly asymmetric in terms of the E plane versus H plane, and the feed taper at the reflector edge is about 10 dB.

The results for the radiated far field of the antenna system in Fig. 10 obtained by the higher order MoM-PO, with the horn antenna in the MoM region and the parabolic reflector in the PO region, are compared with the results obtained by the higher order MoM alone. The simulated co-polarization and cross-polarization normalized patterns in the 45° plane are shown in Fig. 11, and an excellent agreement of the results obtained by the two methods is observed. In particular, the discrepancy in the co-polarization pattern is practically nonexistent for all angles less than almost 50° from the main beam. The maximum discrepancy for angles between 50° and 60° is less than 2 dB for fields that are approximately 50 dB below the field in the main beam, while the only considerable disagreements between the MoM-PO and full MoM results occur in the deep shadow region behind the reflector, for angles between 130° and 180°. In the cross-polarization pattern, a noticeable discrepancy of about 4 dB between the two sets of results at an angle of 35° from the main beam may be attributed to the diffraction of the primary field radiated by the horn feed at the edge of the reflector. However, the cross-polarization field level for this direction is more than 55 dB below the main beam level, which means that this discrepancy is practically negligible as well. Note that the antenna directivity obtained by the higher order MoM-PO, $D_{\mathrm{MoM-PO}} = 36.08$ dBi, agrees perfectly with the result of the rigorous analysis, $D_{\mathrm{MoM}} = 36.12$ dBi.

The total number of unknowns using the two-fold symmetry of the problem is 5458 in both methods. In the pure MoM model, the matrix filling time is 305 s and the LU decomposition takes 504 s. The hybrid MoM-PO solution requires 243 MoM and 5215 PO unknowns. The CPU times for filling the MoM-PO matrices and solving the system of equations are 24 and 7.4 s, respectively, which makes the hybrid higher order analysis more than 25 times faster when compared to the rigorous (full MoM) higher order analysis. Note also that the small-domain technique with RWG basis functions and the use of two-fold symmetry would require more than 33 000 unknowns for the analysis of the same problem.

Fig. 11 also shows the far-field results for a MoM-PO arrangement with a rim in the form of a single layer of MoM patches introduced along the reflector edge. This arrangement requires 943 MoM and 4515 PO unknowns, and 273.09 and 5.76 s of CPU time for the MoM-PO matrix filling and 20 multiple-reflection iterative solution of the system, respectively. A perfect agreement of the MoM-PO results with the MoM solution is observed in this case as a result of an additional accuracy in modeling the currents and fields near the reflector edges.

Finally, shown in Fig. 11 are also the patterns obtained by a "decoupled" version of the higher order MoM-PO in which the effects of the PO currents on the currents in the MoM region are neglected. Although this technique predicts the antenna directivity almost ideally, $D_{\mathrm{MoM-PO\ decoupled}} = 36.00$ dBi, we observe a considerable inaccuracy in the "decoupled" MoM-PO computing of both the co-polarized and cross-polarized patterns apart from the main beam (as compared to the rigorous MoM computation). This is an indication of advantages of the presented ("coupled") higher order MoM-PO simulation over its (much simpler) "decoupled" version in this and similar examples—of course, if the accuracy that it brings is desired. On the other hand, the "decoupled" higher order MoM-PO is certainly a preferable choice in cases where taking into account the mutual interactions between the MoM and PO regions as implemented in this paper does not yield any (significant) improvement to the "decoupled" solution.

IV. Conclusion

This paper has presented an efficient and accurate PC-oriented higher order, large-domain hybrid MoM-PO technique for 3-D analysis of perfectly conducting antennas and scatterers of arbitrary shapes. The technique is based on a system of coupled surface integral equations, with an EFIE in the MoM region and a MFIE in the PO region, and combines higher order geometrical modeling and higher order current modeling in both regions. All the surfaces in the system are modeled by large generalized curvilinear quadrilaterals of arbitrary geometrical orders (large domains). The new technique employs higher order divergence-conforming hierarchical polynomial basis functions in the context of the Galerkin method in the MoM region and higher order divergence-conforming interpolatory basis functions based on modified Chebyshev polynomials in conjunction with a modified point-matching method at the interpolation points of the basis functions in the PO region. This mixed modeling approach optimizes the overall performance of the hybrid method in practical applications.

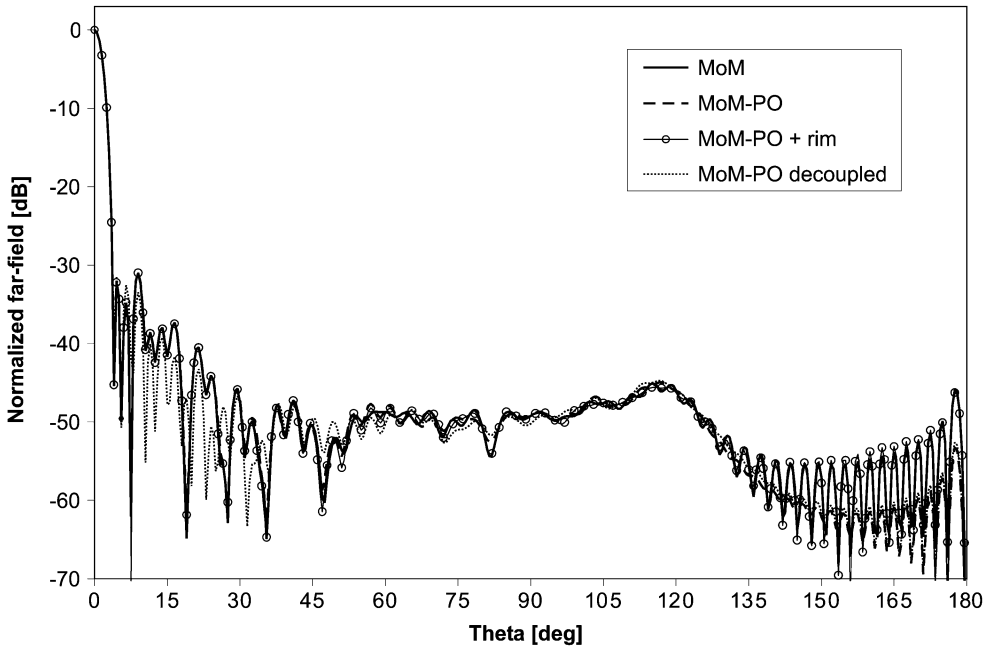

(a)

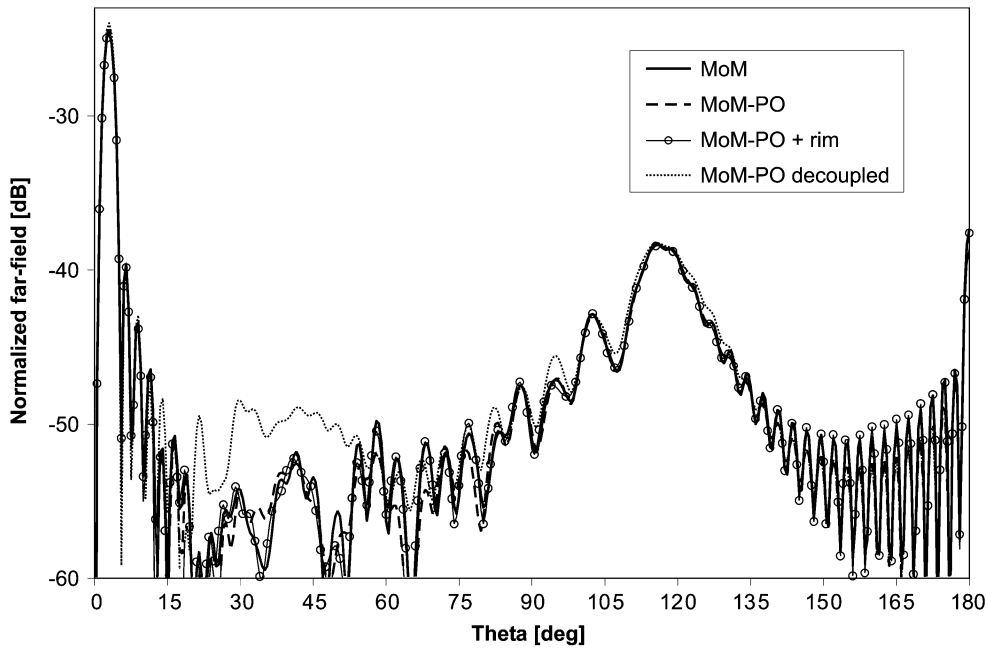

(b)

Fig. 11. Normalized co-polarization (a) and cross-polarization (b) far-field patterns in the 45-degree plane of the antenna in Fig. 10 computed using (1) the full MoM, (2) the MoM-PO with the horn in the MoM region and the reflector in the PO region, (3) the MoM-PO with a rim of MoM patches added around the reflector edge, and (4) the "decoupled" version of the MoM-PO.

The accuracy, efficiency, and versatility of the proposed MoM-PO technique have been demonstrated in three characteristic realistic examples. The results obtained by the higher order MoM-PO have been validated against the results obtained by the full MoM analysis. The truly higher order and large-domain nature of the proposed technique in both MoM and PO regions enables a very substantial reduction in the number of unknowns and increase in accuracy and efficiency when compared to the existing low-order, small-domain MoM-PO techniques. The PO part of the presented technique, on the other hand, has allowed for a dramatic reduction in the computation time and memory requirements with respect to the pure MoM higher order technique, which greatly extends the practicality of the higher order MoM and provides a smooth transition between low- and high-frequency applications.

REFERENCES

[1] R. F. Harrington, "Field computation by moment methods," in *IEEE Series on Electromagnetic Waves*. New York: IEEE, 1993.

[2] G. A. Thiele, "Overview of selected hybrid methods in radiating system analysis," *Proc. IEEE*, vol. 80, no. 1, pp. 66–78, Jan. 1992.

[3] D. P. Bouche, F. A. Molinet, and R. Mittra, "Asymptotic and hybrid techniques for electromagnetic scattering," *Proc. IEEE*, vol. 81, no. 12, pp. 1658–1684, Dec. 1993.
[4] C. S. Kim and Y. Rahmat-Samii, "Low profile antenna study using the physical optics hybrid method (POHM)," in *IEEE Antennas and Propagation Soc. Int. Symp. Dig.*, vol. 3, London, ON, Canada, Jun. 24–28, 1991, pp. 1350–1353.
[5] R. E. Hodges and Y. Rahmat-Samii, "An iterative current-based hybrid method for complex structures," *IEEE Trans. Antennas Propag.*, vol. 45, no. 2, pp. 265–276, Feb. 1997.
[6] ——, "Theory of physical optics hybrid method (POHM)," in *IEEE Antennas Propagation Soc. Int. Symp. Dig.*, vol. 3, Seattle, WA, June 20–24, 1994, pp. 1374–1377.
[7] U. Jakobus, J. Christ, and F. M. Landstorfer, "PO-MoM analysis of cavity-backed antennas," in *Proc. 8th Int. Conf. Antennas and Propagation*, vol. 1, Edinburgh, U.K., Mar.–Apr. 30, 2, 1993, pp. 111–114.
[8] U. Jakobus and F. J. C. Meyer, "A hybrid physical optics/method of moments numerical technique: Theory, investigation and application," in *Proc. IEEE AFRICON'96*, vol. 1, Stellenbosch, South Africa, Sep. 24–27, 1996, pp. 282–287.
[9] U. Jakobus and F. M. Landstorfer, "Improved PO-MM hybrid formulation for scattering from three-dimensional perfectly conducting bodies of arbitrary shape," *IEEE Trans. Antennas Propag.*, vol. 43, no. 2, pp. 162–169, Feb. 1995.
[10] ——, "Improvement of the PO-MoM hybrid method by accounting for effects of perfectly conducting wedges," *IEEE Trans. Antennas Propag.*, vol. 43, no. 10, pp. 1123–1129, Oct. 1995.
[11] F. Obelleiro, J. M. Taboada, J. L. Rodrıguez, J. O. Rubinos, and A. M. Arias, "Hybrid moment-method physical-optics formulation for modeling the electromagnetic behavior of on-board antennas," *Microw. Opt. Technol. Lett.*, vol. 27, no. 2, pp. 88–93, Oct. 20, 2000.
[12] S. M. Rao, D. R. Wilton, and A. W. Glisson, "Electromagnetic scattering by surfaces of arbitrary shape," *IEEE Trans. Antennas Propag.*, vol. 30, no. 3, pp. 409–418, May 1982.
[13] J. M. Taboada, F. Obelleiro, and J. L. Rodrıguez, "Improvement of the hybrid moment method-physical optics method through a novel evaluation of the physical optics operator," *Microw. Opt. Technol. Lett.*, vol. 30, no. 5, pp. 357–363, Sep. 5, 2001.
[14] E. Jørgensen, P. Meincke, and O. Breinbjerg, "A hybrid PO-higher-order hierarchical MoM formulation using curvilinear geometry modeling," in *IEEE Antennas and Propagation Soc. Int. Symp. Dig.*, vol. 4, Columbus, OH, Jun. 22–27, 2003, pp. 98–101.
[15] B. M. Notaroš, M. Djordjević, and M. M. Ilić, "Higher order electromagnetic modeling for wireless technology applications," in *Proc. NSF Wireless Grantees Workshop, IEEE AP-S Topical Conf. Wireless Communications Technology (TCWCT)*, Honolulu, HI, Oct. 15–17, 2003. invited paper.
[16] B. M. Notaroš and B. D. Popović, "Large-domain integral-equation method for analysis of general 3D electromagnetic structures," in *Proc. Inst. Elect. Eng.—Microwaves, Antennas, and Propagation*, vol. 145, Dec. 1998, pp. 491–495.
[17] B. M. Notaroš, B. D. Popović, J. P. Weem, R. A. Brown, and Z. Popović, "Efficient large-domain MoM solution to electrically large practical EM problems," *IEEE Trans. Microw. Theory Techniques*, vol. 49, no. 1, pp. 151–159, Jan. 2001.
[18] M. M. Ilić and B. M. Notaroš, "Higher order hierarchical curved hexahedral vector finite elements for electromagnetic modeling," *IEEE Trans. Microw. Theory Techniques*, vol. 51, no. 3, pp. 1026–1033, Mar. 2003.
[19] M. Djordjević and B. M. Notaroš, "Double higher order method of moments for surface integral equation modeling of metallic and dielectric antennas and scatterers," *IEEE Trans. Antennas Propag.*, vol. 52, no. 8, pp. 2118–2129, Aug. 2004.
[20] ——, "Higher-order hierarchical basis functions with improved orthogonality properties for moment-method modeling of metallic and dielectric microwave structures," *Microw. Opt. Technol. Lett.*, vol. 37, no. 2, pp. 83–88, Apr. 20, 2003.
[21] B. M. Notaroš and B. D. Popović, "Optimized entire-domain moment-method analysis of 3D dielectric scatterers," *Int. J. Numerical Modelling: Electronic Networks, Devices, and Fields*, vol. 10, pp. 177–192, 1997.

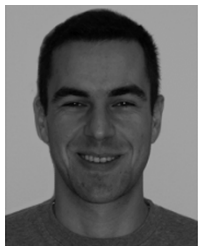

Miroslav Djordjević (S'00–M'04) was born in Ćuprija, Serbia and Montenegro (former Yugoslavia), in 1973. He received the Dipl.Ing. (B.S.) degree from the University of Belgrade, Belgrade, Serbia and Montenegro, in 1998, the M.S. degree from the University of California, Los Angeles (UCLA), in 2000, and the Ph.D. degree from the University of Massachusetts Dartmouth (UMass Dartmouth), in 2004.

From 1998 to 2000, he was a Graduate Student Researcher at Antenna, Research and Measurement (ARAM) Laboratory, UCLA. From 2000 to 2003, he was a Research Assistant at UMass Dartmouth, where he was a Postdoctoral Associate in 2004. He is currently with Antenna Research Associates, Incorporated, Beltsville, MD. His research interests are in higher order modeling, hybrid methods, and analysis and design of ultra wide-band and vehicle mounted antennas.

Branislav M. Notaroš (M'00–SM'03) was born in Zrenjanin, Yugoslavia, in 1965. He received the Dipl.Ing. (B.Sc.), M.Sc., and Ph.D. degrees in electrical engineering from the University of Belgrade, Belgrade, Yugoslavia, in 1988, 1992, and 1995, respectively.

From 1996 to 1998, he was an Assistant Professor in the Department of Electrical Engineering at the University of Belgrade. He spent the 1998–1999 academic year as a Research Associate at the University of Colorado at Boulder. He is currently an Associate Professor of electrical and computer engineering at the University of Massachusetts at Dartmouth. He is a Co-Director of the Telecommunications Laboratory in the Advanced Technology and Manufacturing Center, University of Massachusetts Dartmouth. His research and teaching interests and activities are in theoretical and computational electromagnetics and in antennas and microwaves. His publications include 17 journal papers, 40 conference papers, a book chapter, and five textbooks and workbooks. He is the author of Electromagnetics Concept Inventory, an assessment tool for electromagnetics education.

Dr. Notaroš was the recipient of the 1999 Institution of Electrical Engineers (IEE) Marconi Premium.